JOURNAL OF THERMOPHYSICS AND HEAT TRANSFER
Vol. 16, No. 4, October–December 2002

Heat-Transfer Measurements in Hypersonic Flow Using Luminescent Coating Techniques

J. P. Hubner,* B. F. Carroll,† and K. S. Schanze‡
University of Florida, Gainesville, Florida 32611

The development and application of high-speed imaging and luminescent coating techniques to measure full-field surface heat-transfer rates in short-duration hypersonic flow is presented. Tests were performed on an indented cone model at the 48-in. shock tunnel and the LENS I tunnel facilities at Calspan—University of Buffalo Research Center. Nominal test conditions ranged between Mach numbers of 9.5 and 11.1 and Reynolds numbers of 1.4×10^5 and 3×10^5 m^{-1} with run times of less than 10 ms. Processed submillisecond images show the three-dimensional, time-dependent development of the embedded separated flow and shock/boundary-layer interaction into a steady axisymmetric structure bounded by regions of laminar flow. Conversion from processed image data to full-field heat-transfer measurements were performed using both an in situ calibration with thin-film platinum heat-transfer gauges as well as an a priori temperature calibration and transient heat-transfer theory. In situ calibrations displayed excellent correlation with surface-mounted gauges, whereas a priori calibrations showed a larger susceptibility to bias errors.

Nomenclature

C, D	=	calibration coefficients, K
h	=	coating thickness, μm
I	=	emission intensity
K	=	thermal conductivity, W/K-m
M	=	Mach number
q	=	heat-transfer flux, W/cm^2
Re	=	Reynolds number
T	=	temperature, K
t	=	time, ms or s
U	=	uncertainty
y	=	local depth of temperature-sensitive paint, μm or m
α	=	thermal diffusivity, m^2/s
λ	=	wavelength, nm
τ	=	diffusion time constant, s

Subscripts

cure	=	curing conditions
em	=	emission
ex	=	excitation
i	=	initial conditions
ref	=	reference conditions

Introduction

THE fundamentals of aerodynamic testing with luminescent coatings designated as temperature- and pressure-sensitive paints (TSPs and PSPs, respectively) are well documented.[1,2] The use of luminescent coatings in this context refers to metal-organic luminophors (luminescent molecules) dissolved and processed in a polymer binder to enable the aerosol or casting application of the coating but by nature have an upper temperature limit of 400–500 K. The optical technique yields full-field measurements of the surface temperature, heat transfer, or pressure depending on the composition of the coating. The application of TSPs and PSPs to transient supersonic and hypersonic flow environments, although relatively recent, is increasing.[3–8] For higher temperature ranges, inorganic thermographic phosphors[9–11] and infrared thermometry[12] are alternative techniques.

Basic characteristics of an ideal luminescent-based measurement system for short-duration facilities include durable, fast response coatings; high-energy excitation sources; and high-speed/high dynamic range imaging devices. The primary advantages of such a measurement technique are high spatial resolution, relative non-intrusiveness, and the ease of application/instrumentation compared to point-wise measurement techniques. For instance, the tests presented and discussed in this paper were conducted as part of a larger code validation study of the shock/boundary layer and shock/shock interactions on generic axisymmetric models in laminar hypersonic flow.[13,14] The thin-film heat-transfer sensors employed are well-proven, high-frequency devices but have a physical maximum linear density [Calspan—University of Buffalo Research Center's (CUBRC's) sensor design is about three per cm]. Because of the practical considerations of installation time and cost, the sensors sparsely populate the surface, primarily located to exploit the symmetry of the model with only a few located azimuthally around the cone. When flow asymmetries arise, the initial alignment of sensors might not adequately capture the surface features. With imaging techniques and considering the optical constraints of typical wind-tunnel test facilities and model size, practical pixel (measurement) densities of 100–2500 per cm^2 can be achieved with a 256×256 high-speed imager. The continued development of high-framing rate charge-coupled device (CCD) cameras enables the application of this technique to short-duration (less than 10 ms run time) transient facilities. The focus is on temperature coatings and the subsequent heat-transfer measurements on the indented cone model; however, many of the general characteristics of the coating and equipment apply to pressure measurements in transient and/or high-pressure environments.

Experimental Technique

TSPs are coatings consisting of a carrier, binder, and photoluminescent probes. The carrier is a solvent to enable the dispersion of the probes within the binder and assist in the aerosol application of the paint to the surface of interest. The binder is the matrix that forms the coating, generally oxygen-impermeable polyurethanes,

Received 25 February 2002; revision received 22 May 2002; accepted for publication 22 May 2002.

*Adjunct Assistant Professor, Department of Aerospace Engineering, Mechanics and Engineering Science; also Chief Engineer, AeroChem Corp., P.O. Box 90087, Gainesville, FL 32607; jph@aero.ufl.edu. Member AIAA.

†Associate Professor, Department of Aerospace Engineering, Mechanics and Engineering Science; bfc@aero.ufl.edu. Senior Member AIAA.

‡Professor, Department of Chemistry; kschanze@chem.ufl.edu.

epoxies, or sol-gels. (PSPs use oxygen-permeable binders and quench luminescence via external collisions.) The photoluminescent probes—luminophors—are the temperature-sensitive molecules dispersed within the binder. The temperature sensitivity of the luminophors arises from the competition between photoluminescence and nonradiative relaxation. Photoluminescence is red-shifted from the excitation because of the energy loss processes of internal conversion and crossings between electronic states. The absolute emission intensity is also related to the amount of excitation energy as well as the concentration of the luminophor. For radiometric or intensity-based measurements a reference image is necessary to account for nonuniform coatings and spatially and temporally varying excitation fields.

The proper excitation of the paints depends on the absorption band of the luminophor. Most coatings are designed for long UV to visible blue excitation. The intensity of the coating emission is quantified by an imaging device, that is, a digital camera, appropriately filtered at the emission wavelength. The amount of emission corresponds to gray-scale intensity values on the imager. Images are acquired in the reference and run environments, processed to form an image ratio, and converted to temperature via calibration. The basic processing steps for digital-based imaging, prior to ratioing, are dark-field image correction, flat-field image correction, and image registration or warping. These processes are described in general by Refs. 1 and 2.

Following these processing steps, it might be necessary to correct for the time-dependent nature of the flash source if only a single reference image is used to normalize a sequence of run images. The approach used in these experiments is to acquire a corresponding 1:1 sequence of reference-to-run images in which both sets are triggered at the same relative time within the flash duration. The preceding correction is global in nature and does not account for pixel-by-pixel variation of excitation caused by in- or out-of-plane movement in a nonuniform excitation field. It also assumes stability in the overall excitation field from flash to flash. These issues will be discussed further in the following sections.

The nonradiative decay transition for luminescent probes are often described by an exponential decay process.[15,16] Hence, the corresponding temperature calibration for TSPs follows a logarithmically linear trend with respect to the intensity ratio of reference image to run image [Eq. (1)]:

$$T = C + D\,\ell n\left(\frac{I_{\text{ref,TSP}}}{I_{\text{TSP}}}\right) \tag{1}$$

Ratioing corrects for spatial excitation and coating nonuniformities when the relative specimen movement is small compared to the spatial gradient of the excitation field. Over larger temperature ranges polynomial calibrations might be necessary, but caution should be used when extrapolating beyond the calibrated regions. The calibration coefficients in Eq. (1) are best determined with in situ surface measurements on the model. If calibrating sensors are not available, then an a priori calibration is necessary. Further image processing on calibrated images to improve appearance are spatial filtering and false-color contouring.

Thermal diffusivities of polyurethane binders typically are on the order of 1×10^{-7}–1×10^{-6} m^2/s. Simply based on dimensional analysis, the characteristic response time of TSP coatings is inversely proportional to the thermal diffusivity of the binder [Eq. 2]:

$$\tau \propto h^2/\alpha \tag{2}$$

This response time is slower than the characteristic luminescent lifetime of the luminophor itself by orders of magnitude (0.1–1 ms compared to 0.1–1 μs, respectively, assuming a thin TSP coating of 10 μm or less). Between the active TSP layer and the model surface is an insulating polyurethane layer. The required insulating thickness is estimated based on the one-dimensional, semi-infinite transient heat flow analysis assuming a step change in the heat-transfer rate. This corresponds to an insulator thickness on the order of 100 μm for run times of 10 ms and an insulating diffusivity of 3×10^{-7} m^2/s.

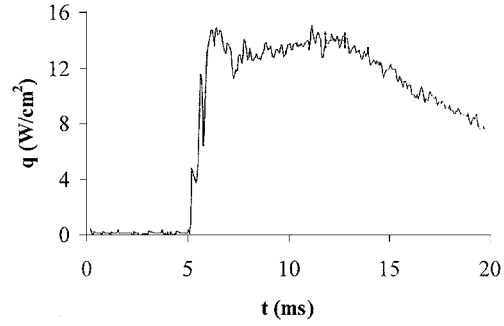

Fig. 1 Typical heat transfer (W/cm^2) vs time (ms) measurement acquired with a CUBRC sensor.

The thin, active TSP layer is sprayed on top of the insulating layer (~5–10 μm). Both the TSP and insulating binders are polyurethane and exhibit similar thermal characteristics except that the TSP has a "thermal" thickness of less than 1% of the insulator. This is important because the purpose of the active TSP layer is to respond to the surface aerodynamic temperature. However, because there is a finite thickness to the active layer a nonuniform temperature distribution through the layer exists. Hence the corresponding integrated intensity through the active TSP layer is an approximate measure of the actual surface intensity. By minimizing the TSP thickness relative to the insulator thickness (while still achieving viable intensity measurements), the integrated induced error as well as the TSP time constant τ is minimized.

For typical short-duration applications presented in this paper, the Biot number (nondimensional heat transfer) and Fourier number (nondimensional time) are small (<0.5). A step change in heat-transfer rate q is assumed. Figure 1 shows a typical point-wise heat-transfer measurement with respect to time. The measured rate is relatively constant until the freestream tunnel conditions deteriorate ($t > 13$ ms). For such conditions q is proportional to the surface temperature rise ΔT (see Appendix).

Facility and Instrumentation

Test Facility

The tests were conducted in the 48-in. shock tunnel and the LENS I tunnel facility at CUBRC. Images of the tunnels' expansion nozzle and test section are shown in Figs. 2a and 2b. The basic operation for each tunnel is the same. The tunnels are started by rupturing a double diaphragm (Fig. 2c), which permits the high-pressure, high-temperature driver gas to travel into the driven tube. A normal shock develops and propagates through the low-pressure driven gas. When the normal shock strikes the end of the driven tube (secondary diaphragm), it is reflected back toward the driver section, leaving a region of nearly stationary high-pressure, high-temperature driven gas. The driven gas is then expanded through a nozzle and into the test section. Run times are controlled by the type of gases, their initial conditions, and the tunnel geometry. Test-section run times are limited by the reflected shock, driver/driven gas interface, or the leading driver expansion wave. Run times can range from a couple of milliseconds up to 30 ms.

TSP and Insulator

The temperature coating uses ruthenium tris (1,10-phenantholine) dichloride (Ru-phen) as the active sensing molecule with the following characteristics: T is 270–400 K; D is 25 K; λ_{ex} is 350–500 nm; λ_{em} is 550–700 nm; t_{cure} is 3 h; and T_{cure} is 315 K. [D is calibration coefficient D in Eq. (1), $T_{ref} = 295$ K, as measured in a temperature controlled spectrophotometer; and the insulator requires same curing time and temperature.] Whereas Ru-phen exhibits oxygen-quenching and hence pressure sensitivity, the luminophors are dissolved into a nonoxygen-permeable polyurethane binder. Figure 3 shows the temperature sensitivity measured with a spectrophotometer. This yields a near-ideal temperature sensitivity because the excitation and emission bandwidths are 1 nm, and

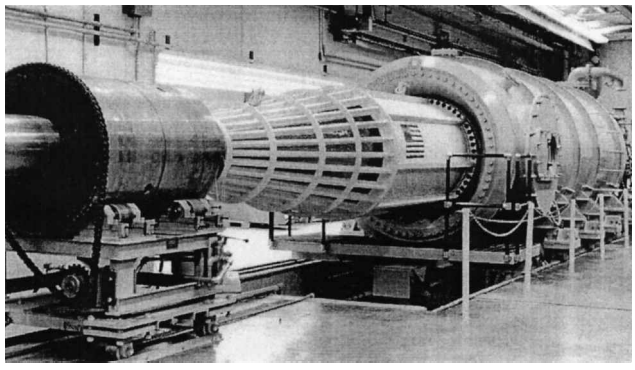

a) LENS I

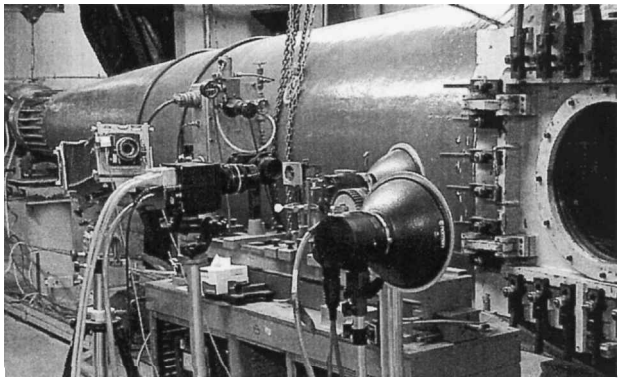

b) 48-in. HST

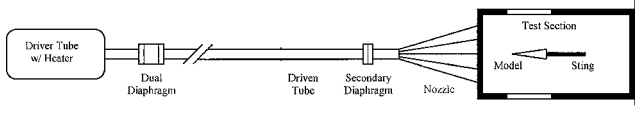

c) Tunnel schematic

Fig. 2 Test facilities and schematic.

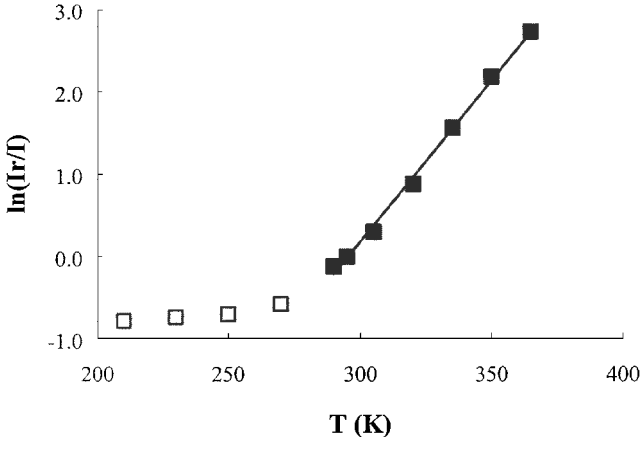

Fig. 3 A priori TSP intensity-ratio calibration using a spectrophotometer: T_{ref} = 295 K. Open symbols represent the low temperature limit of sensitivity.

thus the spectral leakage between excitation and emission is negligible. Maximum sensitivity is in the range of 270–400 K. For lower temperature ranges variants of the ruthenium complex are necessary such as ruthenium bis (2,2′:6′,2″-terpyridine) dichloride (100–200 K) and ruthenium bis (2,2′-bypyridine) (2,2′:6′,2″-terpyridine) dichloride (150–250 K) (unpublished research results by Y. Shen and K. Schanze). At higher temperatures the complex becomes fully quenched, and the polyurethane coating as well as the luminophor is susceptible to thermal degradation. For the more extreme temperature cases high-temperature polyurethanes or binders are required as well as different luminescent probes, including thermographic phosphors.

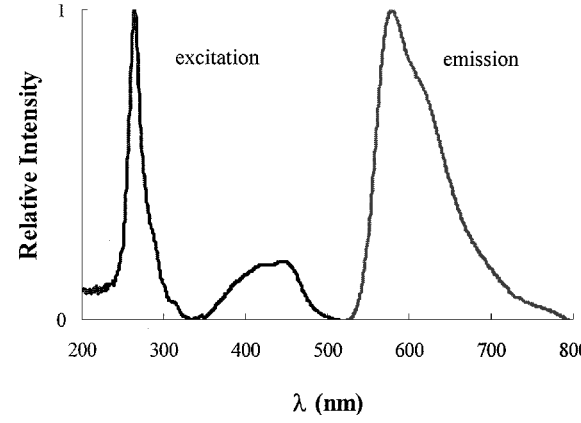

Fig. 4 Relative (to maximum) absorption and emission spectra for the TSP.

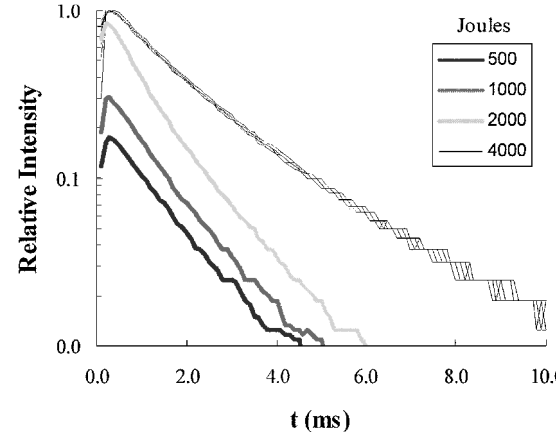

Fig. 5 Relative (to maximum) flash excitation decay for various power settings. The 4000-J setting was repeated eight times to demonstrate flash repeatability.

Visible peak excitation and emission wavelength ranges for the TSP are shown in Fig. 4. The TSP is applied over a white polyurethane insulating layer; both are sprayed using conventional aerosol/airbrush equipment. Nominal TSP and insulator thicknesses are 5–10 μm and 100–150 μm, respectively ($\pm 5\mu$m). Thicknesses were measured with a nonferrous detecting eddy-current probe. The average thermal conductivity and diffusivity of the insulator[17] are 0.48 W/(K-m) and 2.7×10^{-7} m^2/s, respectively, between the temperature range of 293 and 323 K.

Excitation Sources and Filtering

The TSP was excited using a photographic flash unit. The power supply is capable of delivering 4000 J of energy to a single xenon-flash illuminator (2000 J for two illuminators). A power trim dial can adjust to discharge energy down to 125 J. An external relay is used to trigger the flash upon a 5-V timing signal.

As a reasonable approximation, the flash intensity trace follows a simple exponential decay related to 1) the resistance of the flash element and cabling and 2) the variable capacitance set on the power supply. Figure 5 shows characteristic intensity decay plots. (Eight time series are shown for the 4000 J case.) For a single image per test run the flash is set to 2000 J or below. The corresponding time constant is 1.25 ms at 2000 J with a coefficient of variance equal to 3%. For multi-image acquisition, a single flash is set for 4000 J. The corresponding lifetime is 1.93 ms with a coefficient of variance equal to 1%. This level of variance was acceptable to assume constant flash-to-flash excitation, and, hence, the only excitation correction for a sequence of images was the temporal correction caused by the time-dependent decay of the flash. In terms of output energy (98% of total), the relative flash time was 7.9 ms at 4000 J. For longer tunnel

run times multiple units are necessary. The flash is monitored with a photodiode.

Ultraviolet to blue excitation filters and orange-red emission filters are necessary to separate the emission from the excitation. A combination of two Schott glass filters (BG 12 and BG 39; 120 mm o.d. and 3 mm thick) were utilized to filter the xenon flash excitation. Together, they provide excellent filtering of the excitation (see Fig. 6a). For emission filtering a 650-nm interference filter (80-nm bandpass) was used in conjunction with a high-pass Schott glass filter (OG 530; see Fig. 6b). The peak transmission ratio, the ratio of transmitted to incident intensity, for the excitation/emission pair was 8×10^{-8} at 550 nm and 1.4×10^{-7} at 700 nm.

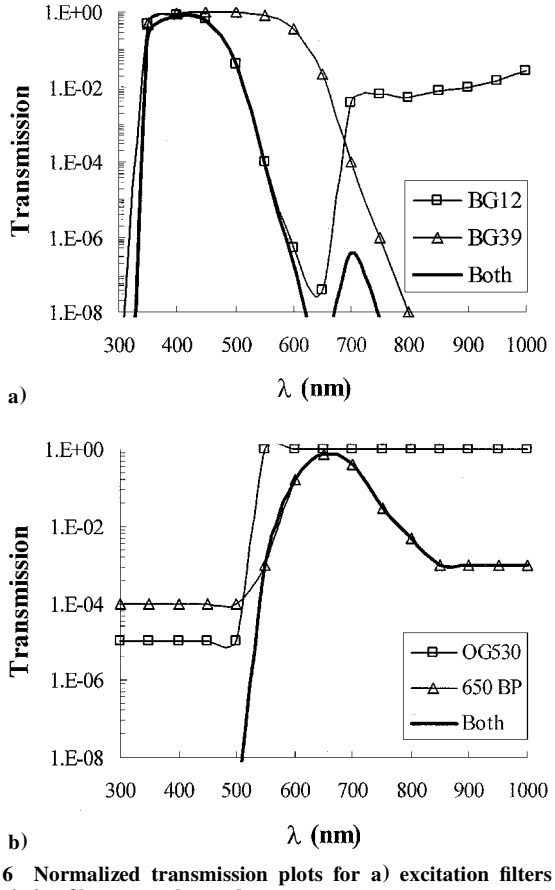

Fig. 6 Normalized transmission plots for a) excitation filters and b) emission filters: note log scale.

CCD Imagers

A fast-framing CCD camera system employs a circuit design that allows on-chip framing rates from 15 frames per second (fps) to 1,000,000 fps with a frame capacity of 17 frames. The practical framing rates for the measurement system used at the CUBRC facilities are 100–5000 fps, depending on the length of the test run, the desired sampling rate, and the ability to effectively detect coating emission for short exposures. In the latter case a high quantum efficiency camera and high luminosity coatings are desirable. The advantage of the flexible framing rate (exposure time) is the ability to choose from a single long-exposure image or several short-exposure images during a single tunnel test. The frames (or images) are stored on the chip until all 17 frames are acquired, then the data are transferred to the PC-installed frame grabber card. The CCD has a full well capacity (FWC) of 220,000 e^- and a readout noise level of 70 e^-. These values correspond to a dynamic range of over 3000; hence, the 12-bit analog-to-digital converter of the frame grabber. The effective spatial resolution per frame is 248×248 pixels, and its active pixel size (fill region) is 13.4×13.4 μm. Features like external triggering and exposure length are software controlled.

In addition to the high-speed imaging, a 14-bit CCD camera (with a SITe SI502A CCD, 512 × 512 pixels) was used. The single-shot camera had better dynamic range and spatial resolution, which is more suitable for time-averaged measurements in a steady-state environment. For both cameras typical photographic lenses were used. Because of the short exposure times, fast lenses are preferred at the expense of depth of field. The *f*/# ranged between 1.4–3.5 with focal lengths of 35–80 mm.

Model and Instrumentation

Figure 7 shows a schematic of the 25/55-deg indented cone model with heat-transfer gauge locations. The back diameter of the model is 0.262 m. The model can be fitted with a sharp- or blunt-nose cap (6.4-mm radius). The overall length with the sharp-nose cap is 0.194 m. Over 60 platinum thin-film heat-transfer gauges are aligned along a ray of the model. Additional gauges were installed azimuthally along the flare (aft) cone near the region of the shock/boundary-layer impingement. The insulating substrate of the gauges is Pyrex. Reported measurement accuracy[13] is ±5%, and the measurement resolution is less than 0.5 W/cm^2.

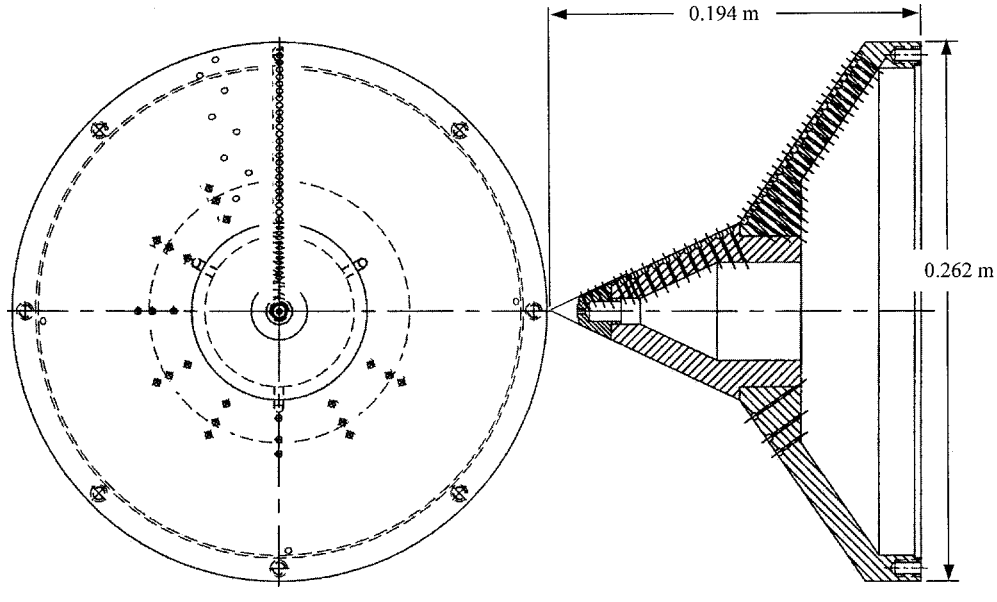

Fig. 7 Schematic of the indented cone model.

The TSP and insulator were applied to 50% of the model for the 48-in. HST tests and 25% of the model for the LENS I tests. For the latter case the azimuthally located heat-transfer gauges limited the region of TSP application. Insulator thickness was 100 μm or greater.

Results and Discussion

The measurements presented and discussed in this paper were part of a larger experimental program used to provide data to evaluate numerical codes for laminar hypersonic flow.[13,14] The Mach-number and Reynolds-number ranges were 9.5–11.1 and 0.14×10^6–0.3×10^6 m^{-1}, respectively. Specific test conditions are listed in Table 1. Figure 8 (Ref. 13, Fig. 37) shows a schlieren photograph of the flowfield around the indented cone model. Visible is the intersection of the forebody shock and the aftbody (flare) shock. There is a separation region induced by the shock/boundary-layer and shock/shock interactions. This exists over the leading cone, and the flow reattaches over the flare cone. Decreasing Mach number and increasing Reynolds number increases the separation size.

Initial TSP measurements were acquired with the single-shot CCD camera in the 48-in. HST. The effective exposure time was 3 ms. The start of the flash was delayed 4 ms beyond the onset of flow. Figures 9a and 9b show in situ calibrated temperature results for runs 41 and 42, respectively. For both cases the separation region and corresponding shock interaction had not stabilized as indicated by the asymmetric high-temperature (light-gray to white) bands formed by the shock/boundary-layer structure aft of the separated region and on the flare cone. (Color images are available via correspondence with authors.) Close inspection of the asymmetry shows that the shock/boundary-layer interaction near the surface corresponds in opposition to the location of the onset of flow separation. Where flow separation is present, the corresponding surface temperature (or heat-transfer rate) is low (dark gray). As the onset of the separation region occurs further upstream, the shock interaction with the boundary layer occurs further downstream.

The asymmetric flow features shown in Fig. 9 were transient in nature and stabilized after 6–8 ms. (Freestream test conditions are attained approximately 2 ms from the onset of flow.) Figure 10, an in-situ calibrated heat-transfer image from run 25, shows a stabilized axisymmetric pattern. Clearly present are the separated (dark gray) and shock/boundary-layer interaction (light gray) regions. Figure 11 shows centerline heat-transfer values for both the TSP and gauge measurements. Visible in the line graph and the grayscale contours is the mild recompression aft of the shock/boundary-layer interaction. The relative rms calibration error of the TSP measurements with the gauge measurements is 15%. This variation is caused by the high-frequency unsteadiness in the flow features as detected by the heat-transfer gauges. The standard deviation of the calibrating gauge measurements relative to the mean (acquired over 1–2 ms) ranged from 10 to 20% with the higher variations in the region near the shock/boundary-layer interactions.

Figure 12 shows the time-dependent intensity-ratio images captured with the high-speed camera (run 46). The framing rate was 2000 fps (0.5 ms exposure). Every other intensity-ratioed image is shown (1 ms). Reviewing the image sequence from left to right shows the development of the surface heating. The first image is 1 ms aft the onset of flow. This image and the following, acquired while the tunnel conditions rise to the desired freestream conditions, shows the flare shock impingement just aft of the intersection of the leading and flare cones. Afterwards, the separation region grows upstream, and the shock impingement moves downstream. At 4 ms the azimuthal boundary of the shock impingement is similar to that shown in Fig. 9. A spatial waviness of two periods per circumference

Table 1 Run matrix

Run	M	Re, 1/m	Nose	Facility
41	11.1	0.14×10^6	Sharp	48-in. HST
42	11.1	0.16×10^6	Blunt	48-in. HST
46	11.0	0.14×10^6	Sharp	48-in. HST
25	9.6	0.27×10^6	Sharp	LENS I

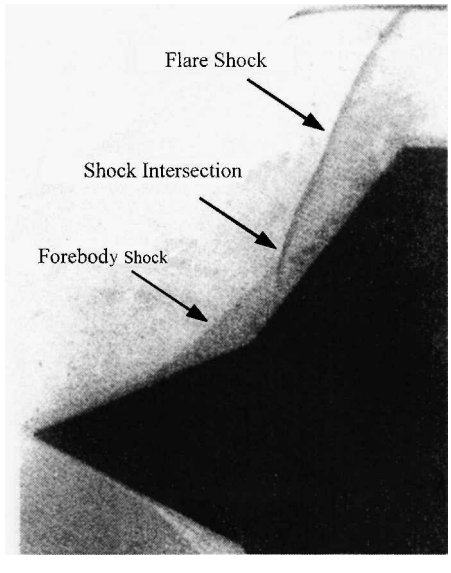

Fig. 8 Schlieren photograph of flow over the indented cone model (from Ref. 13, Fig. 37).

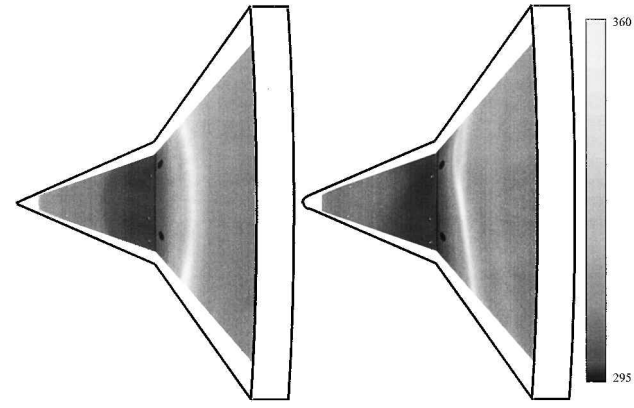

Fig. 9 Temperature results for the sharp-nose (left) and blunt-nose (right) indented cone model in the 48-in. HST with a 4-ms delay from flow onset. Asymmetric features were captured prior to the flow structure stabilizing at ~ 7–8 ms.

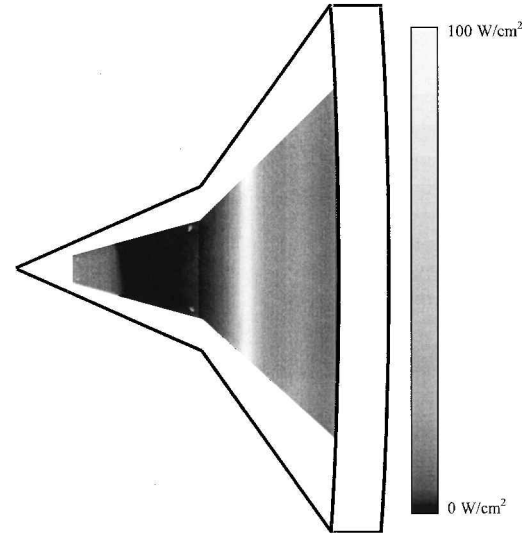

Fig. 10 Heat-transfer results for the sharp-nose indented cone model in LENS I with an 8-ms delay from flow onset.

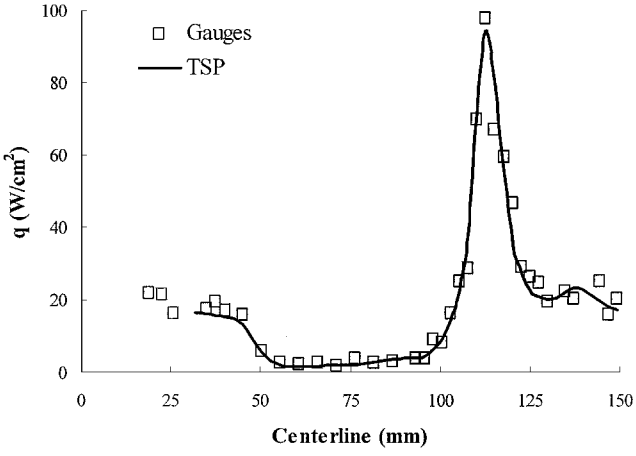

Fig. 11 Centerline heat-transfer results from Fig. 10.

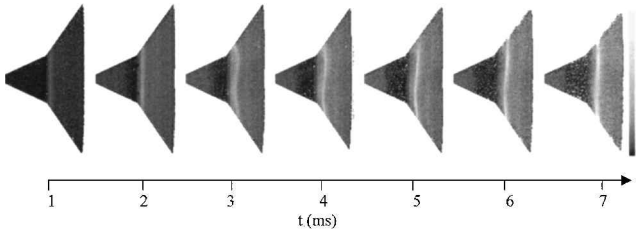

Fig. 12 Time-dependent intensity-ratio measurements on the sharp-nose indented cone. Images shown at successive 1-ms intervals. (Actual acquisition rate was 2000 fps.)

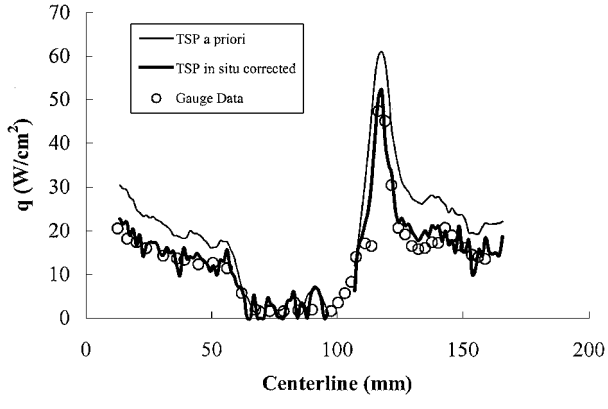

Fig. 13 Centerline heat-transfer results from Fig. 12.

exists. As time increases, the separated region and shock impingement boundary appear to stabilize and become axisymmetric.

Figure 13 shows the corresponding heat-transfer results from the time-dependent intensity ratio data (Fig. 12) along the centerline of the model. First, the intensity-ratio data were converted to heat-transfer measurements using an a priori intensity/temperature calibration (Fig. 3), the thermal properties of the coating, and the transient one-dimensional heat-transfer assumptions described earlier. As shown by the thin line, the trends match that of the gauge measurements, but the coating values overpredicted the gauge measurements by 20–50%. Often the case with a priori calibrations is the presence of unacceptable bias or offset errors. These arise as a result of 1) the differences between the coating calibration experiments and the actual applied experiments (test setup differences that lead to spectral leakage, background illumination, etc.) and 2) uncertainties associated with the thermal properties of the coating and insulator. For the latter case the uncertainty in the thermal diffusivity and conductivity is 9 and 6%, respectively.[17] Although these errors arise as biases, they would not account for the overall bias in the a priori calculations. It is the former case, where calibrating conditions have changed (broader spectral filtering ranges, possible spectral leakage, and finite TSP thicknesses), that causes the larger offset. In situ calibration with gauge measurements can account for these bias errors. When the intensity-ratio data are calibrated with the gauge data (thick line), there is excellent agreement. Calculations based on time-dependent measurements show a minimum resolution of approximately 2–3 W/cm^2.

Conclusions

This paper describes the application of time-dependent TSP measurement techniques to acquire the surface temperature and heat-transfer rates on a generic indented cone configuration in short-duration hypersonic flow. Freestream Mach numbers ranged between 9.5 and 11.1 and run times were on the order of 10 ms. Heat-transfer rates ranged between 1 and 100 W/cm^2. The measurement technique demonstrated its value by clearly capturing the initial time-dependent nature of the surface features during the onset of flow and then the final axisymmetric distribution. Intensity ratio measurements calibrated well with in situ surface mounted gauges; however, a priori calibrations led to large bias errors. Heat-transfer measurements were determined from both single-shot and time-dependent image data. A practical camera exposure time of 0.5 ms was used to balance the effects of low measurement intensity and provide reasonable temporal resolution. The threshold measurement resolution was 2–3 W/cm^2. Further advances in CCD or camera technology that increase the number of captured frames without sacrificing outlined performance characteristics are desirable; however, this must correspond to improved or multiple excitation sources (preferably constant intensity) that enable longer overall acquisition times.

Appendix: Additional Theory

Heat-Transfer Rate Calculation

The temperature distribution for a one-dimensional, semi-infinite layer, constant heat-transfer analysis[18] is shown in Eq. (A1):

$$T(t, y) = T_i + \frac{2q\sqrt{\alpha t/\pi}}{k}\exp\left(\frac{-y^2}{4\alpha t}\right) - \frac{qy}{k}\operatorname{erfc}\left(\frac{y}{2\sqrt{\alpha t}}\right) \quad \text{(A1)}$$

At the surface ($y = 0$) the change in the square of the temperature rise, $\Delta T^2 = (T_{y=0} - T_i)^2$, with respect to time is constant assuming that the thermal properties k and α are independent of temperature. Hence,

$$\left.\frac{\mathrm{d}\Delta T^2}{\mathrm{d}t}\right|_{y=0} = \frac{4}{\pi}\frac{q^2\alpha}{k^2} = \text{const} \quad \text{(A2)}$$

From Eq. (1), the TSP calibration equation, the change in temperature is

$$\Delta T = T - C = D\,\ell n(I^*) \quad \text{(A3)}$$

where I^* is the intensity ratio of the reference condition to the run condition and $\Delta T = 0$ when $I^* = 1$ at $t = 0$. Substituting Eq. (A3) into Eq. (A2) yields

$$\left.\frac{\mathrm{d}\Delta T^2}{\mathrm{d}t}\right|_{y=0} = \frac{D^2\,\ell n^2(I^*)}{t} = \frac{4}{\pi}\frac{q^2\alpha}{k^2} \quad \text{(A4)}$$

and rearranging results in the following expression for q:

$$q = \sqrt{\frac{\pi}{4\alpha}}kD\left[\frac{\ell n(I^*)}{\sqrt{t}}\right] \quad \text{(A5)}$$

For multi-image sequences with respect to time, a least-square regression can be used to calculate the expression in the square brackets. In cases of transient heat flux, numerical integration of the time-dependent data is necessary.[19,20]

Uncertainty Analysis

A general uncertainty analysis[21] on Eq. (A5) provides some insight on the relative contribution of each term to the total uncertainty in the calculation of q. Equation (A6) shows the resulting relative uncertainty in terms of the uncertainty in k, α, ΔT, and t:

$$\frac{U_q}{q} = \sqrt{\left(\frac{U_k}{k}\right)^2 + \left(\frac{U_{\Delta T}}{\Delta T}\right)^2 + \frac{1}{4}\left(\frac{U_\alpha}{\alpha}\right)^2 + \frac{1}{4}\left(\frac{U_t}{t}\right)^2} \quad \text{(A6)}$$

Assuming the temperature calibration constant D is determined in situ, the uncertainty in ΔT arises as a result of the uncertainty in the camera intensity measurements. Based on the TSP calibration [Eq. (1)] the relative uncertainty in ΔT is

$$U_{\Delta T}/\Delta T = [1/\ell n(I^*)]\left[U_{I^*}/I^*\right] \quad \text{(A7)}$$

Equations (A6) and (A7) show that the intensity-ratio uncertainty and the thermal conductivity uncertainty are the most important contributions. Specifically, when there is a small temperature change there is a significant contribution in uncertainty caused by the functional form of Eq. (A7). Small changes in temperature correspond to values of $I^* \approx 1$; hence, $\ell n(I^*) \approx 0$, and the uncertainty in the temperature change is large. As the temperature change increases (as a result of higher heat-transfer rates, longer measurement times, or changes in the insulator properties), the associated uncertainty decreases. Relative uncertainty values for the various contributing parameters presented in this paper are 9% for thermal conductivity, 6% for thermal diffusivity, and 2% for time. As just explained, the relative uncertainty in the temperature depends on the amount of temperature change. Based on the contributing factors of shot noise, readout noise, and A/D resolution, and assuming 25% full-well capacity for both the reference and run images, the temperature change uncertainty ranges between 46% for $\Delta T = 1$ K and 2% for $\Delta T = 20$ K. For the latter case the heat-transfer uncertainty is 10% and is primarily caused by the uncertainty in the thermal conductivity. In situ calibration can account for the uncertainties of k and α, and, thus, the relative uncertainty is controlled by the camera and excitation characteristics (~3%).

Acknowledgments

Research presented in this paper was funded by a Phase II Small Business Innovative Research (SBIR) contract with the U.S. Army Aviation and Missile Command (DAAH01-97-C-R009). William Walker was the Contract Monitor for the SBIR contract, and Michael Holden was the Technical Monitor with CUBRC. Special thanks are given to Gary Paone and Richard Bergman of CUBRC as well as Gary Dale of Wright–Patterson Air Force Base for the initial loan/use of the high-speed camera.

References

[1]Liu, T., Campbell, B. T., Burns, S. P., and Sullivan, J. P., "Temperature- and Pressure-Sensitive Luminescent Paints in Aerodynamics," *Applied Mechanics Review*, Vol. 50, No. 4, 1997, pp. 227–246.

[2]Bell, J. H., Schairer, E. T., Hand, L. A., and Mehta, R. D., "Surface Pressure Measurements Using Luminescent Coatings," *Annual Review of Fluid Mechanics*, Vol. 33, 2001, pp. 155–206.

[3]Borovoy, V., Bykov, A., Mosharov, V., Orlov, A., Radchenko, V., and Fonov, S., "Pressure Sensitive Paint Application in Shock Wind Tunnel," *16th ICIASF Record*, Inst. of Electrical and Electronics Engineers, New York, 1995, pp. 34.1–34.4.

[4]Liu, T., Campbell, B. T., and Sullivan, J. P., "Fluorescent Paint for Measurement of Heat Transfer in Shock-Turbulent Boundary Layer Interaction," *Experimental Thermal and Fluid Science*, Vol. 10, No. 1, 1995, pp. 101–112.

[5]Liu, T., Campbell, B. T., Sullivan, J. P., Lafferty, J., and Yanta, W., "Heat Transfer Measurement on a Waverider at Mach 10 Using Fluorescent Paint," *Journal of Thermophysics and Heat Transfer*, Vol. 9, No. 4, 1995, pp. 605–611.

[6]Hubner, J. P., Carroll, B. F., Schanze, K. S., and Ji, H. F., "Pressure-Sensitive Paint Measurements in a Shock Tube," *Experiments in Fluids*, Vol. 28, No. 1, 2000, pp. 21–28.

[7]Hubner, J. P., Carroll, B. F., Schanze, K. S., Ji, H. F., and Holden, M. S., "Temperature and Pressure-Sensitive Paint Measurements in Short-Duration Hypersonic Flow," *AIAA Journal*, Vol. 39, No. 4, 2001, pp. 654–659.

[8]Winslow, N. A., Carroll, B. F., and Kurdila, A. J., "Model Development and Analysis of Dynamics of Pressure-Sensitive Paints," *AIAA Journal*, Vol. 39, No. 4, 2001, pp. 660–666.

[9]Allison, S. W., and Gillies, G. T., "Remote Thermometry with Thermographic Phosphors: Instrumentation and Applications," *Review of Scientific Instruments*, Vol. 68, No. 7, 1997, pp. 2615–2650.

[10]Buck, G. M., "Simultaneous Global Pressure and Temperature Measurement Technique for Hypersonic Wind Tunnels," AIAA Paper 2000-2649, June 2000.

[11]Buck, G. M., "Surface Temperature/Heat Transfer Measurement Using a Quantitative Phosphor Thermography System," AIAA Paper 94-2482, June 1994.

[12]Hakenesch, P. R., "Thin Layer Thermography—A New Heat Transfer Measurement Technique," *Experiments in Fluids*, Vol. 26, No. 3, 1999, pp. 257–265.

[13]Holden, M. S., and Wadhams, T. P., "Code Validation Study of Laminar Shock/Boundary Layer and Shock/Shock Interactions in Hypersonic Flow—Part A: Experimental Measurements," AIAA Paper 2001-1031, Jan. 2001.

[14]Harvey, J. K., Holden, M. S., and Wadhams, T. P., "Code Validation Study of Laminar Shock/Boundary Layer and Shock/Shock Interactions in Hypersonic Flow—Part B: Comparison with Navier–Stokes and DSMC Solutions," AIAA Paper 2001-1031, Jan. 2001.

[15]Caspar, J. V., "Excited State of Decay of Processes in Osmium(II), Ruthenium(II), and Rhenium(II) Polypyridyl Complexes," Ph.D. Dissertation, Dept. of Chemistry, Univ. of North Carolina, Chapel Hill, NC, 1982.

[16]Van Houten, J., and Watts, R., "Temperature Dependence of Photophysical and Photochemical Properties of the Tris(2,2′-dipyridyl)ruthenium(II) Ion in Aqueous Solution," *Journal of American Chemical Society*, Vol. 98, No. 6, 1976, pp. 4853–4858.

[17]Campbell, D. C., "Thermal Diffusivity, Specific Heat, and Thermal Conductivity of a Polyurethane Coating," Holometrix Micromet, Rept. AEH-1, Bedford, MA, Feb. 2001.

[18]Incropera, F. P., and Dewitt, D. P., *Fundamentals of Heat Transfer*, 1st ed., Wiley, New York, 1981, pp. 204–208.

[19]Cook, W. J., and Felderman, E. J., "Reduction of Data from Thin-Film Heat Transfer Gages: A Concise Numerical Technique," *AIAA Journal*, Vol. 4, No. 3, 1966, pp. 561, 562.

[20]George, W. K., Rae, W. J., and Woodward, S. H., "An Evaluation of Analog and Numerical Techniques for Unsteady Heat Transfer Measurement with Thin-Film Gauges in Transient Facilities," *Experimental Thermal and Fluid Science*, Vol. 4, No. 3, 1991, pp. 333–342.

[21]Coleman, H. W., and Steele, W. G., *Experimentation and Uncertainty Analysis for Engineers*, 1st ed., Wiley, New York, 1989, pp. 40–52.